



A New Model of Jupiter's Magnetic Field at the Completion of Juno's Prime Mission

Connerney, J. E. P.; Timmins, S.; Oliverson, R. J.; Espley, J. R.; Joergensen, J. L.; Kotsiaros, S.; Joergensen, P. S.; Merayo, J. M. G.; Herceg, M.; Bloxham, J.

Total number of authors:
15

Published in:
Journal of Geophysical Research: Planets

Link to article, DOI:
[10.1029/2021JE007055](https://doi.org/10.1029/2021JE007055)

Publication date:
2022

Document Version
Publisher's PDF, also known as Version of record

[Link back to DTU Orbit](#)

Citation (APA):

Connerney, J. E. P., Timmins, S., Oliverson, R. J., Espley, J. R., Joergensen, J. L., Kotsiaros, S., Joergensen, P. S., Merayo, J. M. G., Herceg, M., Bloxham, J., Moore, K. M., Mura, A., Moirano, A., Bolton, S. J., & Levin, S. M. (2022). A New Model of Jupiter's Magnetic Field at the Completion of Juno's Prime Mission. *Journal of Geophysical Research: Planets*, 127(2), Article e2021JE007055. <https://doi.org/10.1029/2021JE007055>

General rights

Copyright and moral rights for the publications made accessible in the public portal are retained by the authors and/or other copyright owners and it is a condition of accessing publications that users recognise and abide by the legal requirements associated with these rights.

- Users may download and print one copy of any publication from the public portal for the purpose of private study or research.
- You may not further distribute the material or use it for any profit-making activity or commercial gain
- You may freely distribute the URL identifying the publication in the public portal

If you believe that this document breaches copyright please contact us providing details, and we will remove access to the work immediately and investigate your claim.

A New Model of Jupiter's Magnetic Field at the Completion of Juno's Prime Mission



Key Points:

- The Juno spacecraft sampled Jupiter's vector magnetic field along 32 polar passes separated by $\sim 11^\circ$ longitude at the equator
- A degree 18 spherical harmonic model of Jupiter's magnetic field is obtained by partial solution of a degree 30 linear system
- The new model is consistent with dynamo action in metallic hydrogen, advection of the field by deep zonal winds, and secular variation

Supporting Information:

Supporting Information may be found in the online version of this article.

Correspondence to:

J. E. P. Connerney,
jack.connerney@nasa.gov

Citation:

Connerney, J. E. P., Timmins, S., Oliverson, R. J., Espley, J. R., Joergensen, J. L., Kotsiaros, S., et al. (2022). A new model of Jupiter's magnetic field at the completion of Juno's Prime Mission. *Journal of Geophysical Research: Planets*, 127, e2021JE007055. <https://doi.org/10.1029/2021JE007055>

Received 8 SEP 2021
Accepted 15 DEC 2021

Author Contributions:

Conceptualization: J. M. G. Merayo, J. Bloxham, K. M. Moore

Formal analysis: S. Timmins, J. R. Espley, J. L. Joergensen, S. Kotsiaros, P. S. Joergensen, J. M. G. Merayo, M. Herceg, K. M. Moore

Funding acquisition: S. J. Bolton, S. M. Levin

Investigation: J. R. Espley, J. L. Joergensen, S. Kotsiaros, P. S. Joergensen, J. M. G. Merayo, M. Herceg, J. Bloxham, K. M. Moore, A. Mura, A. Moirano, S. J. Bolton, S. M. Levin

© 2021 The Authors.

This is an open access article under the terms of the [Creative Commons Attribution-NonCommercial License](https://creativecommons.org/licenses/by-nc/4.0/), which permits use, distribution and reproduction in any medium, provided the original work is properly cited and is not used for commercial purposes.

J. E. P. Connerney^{1,2} , S. Timmins^{2,3}, R. J. Oliverson² , J. R. Espley² , J. L. Joergensen⁴, S. Kotsiaros⁴ , P. S. Joergensen⁴ , J. M. G. Merayo⁴ , M. Herceg⁴ , J. Bloxham⁵ , K. M. Moore⁶ , A. Mura⁷ , A. Moirano⁷ , S. J. Bolton⁸ , and S. M. Levin^{6,9} 

¹Space Research Corporation, Annapolis, MD, USA, ²NASA Goddard Space Flight Center, Greenbelt, MD, USA, ³ADNET Systems, Inc., Bethesda, MD, USA, ⁴Technical University of Denmark (DTU), Kongens Lyngby, Denmark, ⁵Harvard University, Cambridge, MA, USA, ⁶California Institute of Technology, Pasadena, CA, USA, ⁷INAF-IAPS, Rome, Italy, ⁸Southwest Research Institute, San Antonio, TX, USA, ⁹Jet Propulsion Laboratory (JPL), Pasadena, CA, USA

Abstract A spherical harmonic model of the magnetic field of Jupiter is obtained from vector magnetic field observations acquired by the Juno spacecraft during 32 of its first 33 polar orbits. These Prime Mission orbits sample Jupiter's magnetic field nearly uniformly in longitude ($\sim 11^\circ$ separation) as measured at equator crossing. The planetary magnetic field is represented with a degree 30 spherical harmonic and the external field is approximated near the origin with a simple external spherical harmonic of degree 1. Partial solution of the underdetermined inverse problem using generalized inverse techniques yields a model ("JRM33") of the planetary magnetic field with spherical harmonic coefficients reasonably well determined through degree and order 13. Useful information regarding the field extends through degree 18, well fit by a Lowes' spectrum with a dynamo core radius of $0.81 R_J$, presumably the outer radius of the convective metallic hydrogen region. This new model provides a most detailed view of a planetary dynamo and evidence of advection of the magnetic field by deep zonal winds in the vicinity of the Great Blue Spot (GBS), an isolated and intense patch of flux near Jupiter's equator. Comparison of the JRM33 and JRM09 models suggests secular variation of the field in the vicinity of the GBS during Juno's nearly 5 years of operation in orbit about Jupiter. The observed secular variation is consistent with the penetration of zonal winds to a depth of $\sim 3,500$ km where a flow velocity of $\sim 0.04 \text{ ms}^{-1}$ is required to match the observations.

Plain Language Summary Characterizing the planetary magnetic field of Jupiter is one of the primary science objectives of the Juno Mission. Is the magnetic field generated within the outer envelope consisting mostly of molecular hydrogen, or is it generated at depth where hydrogen becomes metallic under great pressure? The Juno spacecraft, in polar orbit about Jupiter since July 2016, just completed its baseline mapping mission of 33 orbits, providing global coverage of Jupiter's magnetic field near the planet. A detailed representation of the field has emerged, suggesting that Jupiter's magnetic field is generated by dynamo action at depth (beneath $0.81 R_J$) in convective metallic hydrogen. A change in Jupiter's magnetic field over time ("secular variation") was identified by comparison of the model field with that of an earlier model. The secular variation appeared on the flanks of an isolated magnetic patch (the "Great Blue Spot" (GBS)) and can be explained by the eastward motion of the field of the GBS, carried by zonal winds at a depth ($\sim 3,500$ km) where molecular hydrogen is sufficiently electrically conductive to grip the magnetic field.

1. Introduction

The Juno mission was designed, in part, to map Jupiter's magnetic field with extraordinary accuracy using an assemblage of close polar passages to approximate global coverage on a surface enclosing the planet (Bolton, Lunine, et al., 2017; Connerney et al., 2017). A potential field is (in theory) uniquely determined by noise-free vector observations on a closed surface about the source. Thus, magnetic mapping missions are often designed to provide near-circular polar orbits that over time distribute observations on a spherical surface enclosing the source. The Juno mission approximates global coverage with the close polar passages of highly elliptical orbits equally spaced in longitude about the planet. During the Prime Mission, Juno acquired science observations near Jupiter on 32 of 33 highly elliptical 53-day orbits with perijoves of $\sim 1.05 R_J$ (Jupiter radius, $1 R_J = 71,492$ km) and apojoves of $\sim 113 R_J$. Juno targeted specific longitudes on each pass via slight adjustments to the orbit period. The mission plan was designed to provide coarse global coverage initially, with perijoves separated by 90° after 4

Project Administration: R. J. Oliverson, S. J. Bolton, S. M. Levin
Resources: R. J. Oliverson, A. Mura, A. Moirano
Software: S. Timmins, M. Herceg
Validation: J. R. Espley, S. Kotsiaros, P. S. Joergensen, J. M. G. Merayo, M. Herceg, J. Bloxham
Visualization: S. Timmins, S. Kotsiaros, P. S. Joergensen

orbits, followed by more closely spaced perijoves (45° separation after 8 orbits, 22.5° after 16 orbits, and 11.25° after 32 orbits). Data was not acquired during the second perijove (PJ2) following a spacecraft safing event. Dense global coverage was achieved after the 33rd perijove (PJ33) on 15 April 2021, with $\sim 11^\circ$ longitudinal separation between orbits measured at descending (post-perijove) equator crossing.

Juno's first 9 orbits provided enough global coverage to greatly improve upon models of Jupiter's magnetic field, yielding an interim model (Connerney et al., 2018) of the field characterized by a degree 10 spherical harmonic ("JRM09," Jupiter Reference Model after 9 orbits). The superior distribution of observations afforded by the Juno trajectory offered a great improvement in spatial resolution compared to prior models obtained from the limited and more distant flybys of earlier missions (Connerney, 2015; Connerney et al., 1998; Hess et al., 2011; Ridley & Holme, 2016). The JRM09 model described a magnetic field of surprising complexity that was anticipated after the very first close passage over the planet's surface revealed a surprising departure from existing models (Bolton, Adriani, et al., 2017; Moore et al., 2017). That feature became known as the "Great Blue Spot," an intense and localized patch of flux near the equator near 90° System III longitude (Moore et al., 2018) that has become a focal point of discussions regarding secular variation of the main (internal) field (Moore et al., 2019).

The JRM09 magnetic field model was proposed as an interim model, recognizing that with but 8 close polar passages, the field was significantly undersampled in longitude. Those 8 orbits crossed the equator separated by 45° in longitude, which equates to a separation of $0.8 R_J$ between them. Thus, the spacecraft was much closer to the presumptive dynamo source region (e.g., $\sim 0.8 R_J$) than it was to adjacent passes. At the completion of the Primary Mission, the 32 periapsis passes available now are separated by $\sim 11^\circ$ in longitude, which equates to a pass-to-pass separation of $\sim 0.2 R_J$ at equator crossing, comparable to the depth to the source region. In this paper we describe an improved magnetic field model derived from Juno's Prime Mission orbits; the increased density of observations provides for a model with greater resolution of the field and offers insight regarding the Jovian dynamo and secular variation of the field. Juno's extended mission will continue to increase the density of observations in longitude and map the magnetic field above the all-important Great Blue Spot early in extended mission. Perijoves continue to move steadily northward during the extended mission affording close-in observations over the most intense magnetic fields at northern mid-latitudes.

2. Methods

The magnetic field observed very near Jupiter is dominated by the field due to dynamo action inside Jupiter, with relatively minor contributions from distributed magnetospheric currents (Connerney et al., 1981, 2020) and Birkeland currents (Kotsiaros et al., 2019). As we will only use observations acquired close to the planet, in a current-free region (but for Birkeland currents encountered at high latitudes, negligible in the present context) we may obtain the magnetic field from the gradient of a scalar potential function V ,

$$\mathbf{B} = -\nabla V$$

where V is represented by a spherical harmonic expansion (e.g., Chapman & Bartels, 1940);

$$V = a \sum_{n=1}^{N_{max}} \left\{ \left(\frac{a}{r} \right)^{n+1} \sum_{m=0}^n \{ P_n^m(\cos\theta) [g_n^m \cos(m\phi) + h_n^m \sin(m\phi)] \} + \left(\frac{r}{a} \right)^n \sum_{m=0}^n \{ P_n^m(\cos\theta) [G_n^m \cos(m\phi) + H_n^m \sin(m\phi)] \} \right\}$$

and a is Jupiter's equatorial radius (71,492 km), r is the radial distance to the planet's center, and the angles θ and ϕ are colatitude and longitude, respectively. Internal sources are parameterized via Schmidt coefficients (g_n^m , h_n^m) associated with inverse powers of r and sources external to the region of measurement are parameterized via coefficients (G_n^m , H_n^m) associated with increasing powers of r ; the $P_n^m(\cos\theta)$ are Legendre functions of degree n and order m . Coefficients are given in units of nanoteslas ($1G = 10^5$ nT) for a particular choice of planet radius.

We assume here that the planetary magnetic field remains constant over the interval of time (27 August 2016 through 15 April 2021) spanned by the first 33 perijoves, and that Jupiter's rotation period ($870.5360^\circ/\text{day}$) describes the rigid rotation of the deep interior. Analysis of gravity observations suggests that while zonal winds extend to a few thousand kilometers depth, the deep interior does rotate as a rigid body (Guillot et al., 2018).

Assuming the magnetic field has remained constant over the nearly 5 years it has taken to accumulate 33 orbits is questionable, particularly considering Moore et al.'s analysis (2019) of observations acquired during the Pioneer, Voyager, and Ulysses flybys dating back to the early 1970's. The secular variation of the field deduced by Moore et al. appears localized to the equatorial Great Blue Spot where the radial field may vary by as much as ~ 0.14 Gauss/yr at the surface. The time variation may be explained by advection of the intense radial field of the GBS (~ 12 Gauss at the surface) by deep zonal winds (Moore et al., 2019). Confinement of the time variable part of the field to a small fraction of the sphere makes representation in terms of time dependent spherical harmonics very inefficient and impractical, and beyond the scope of this effort.

The external field is dominated by the magnetodisc (Connerney et al., 2020), which produces a nearly uniform field of order 100 nT near the origin; that, and fields produced by more distant currents, may be approximated conveniently by a uniform magnetic field (external spherical harmonic of degree 1) within $2.5 R_J$ of the origin. The magnetodisc field has demonstrated remarkable stability over the first 24 Juno orbits (Connerney et al., 2020) and its variation in time is negligible in the present context. Birkeland currents are detected during some polar passages, and may contribute fields of a few hundred nT (Kotsiaros et al., 2019), but their signatures are narrowly confined and relatively weak (few 0.1% of the total field). They are unlikely to significantly bias estimation of internal field parameters.

The model parameters are found solving the linear system $\mathbf{y} = \mathbf{A} \mathbf{x}$ relating the observations (\mathbf{y}) to the model parameters (\mathbf{x}). The column vector \mathbf{y} is comprised of the three components of the vector field at each observation point, and the column vector \mathbf{x} is a list of the spherical harmonic coefficients. The singular value decomposition (Connerney, 1981; Lanczos, 1961) is used to factor the matrix \mathbf{A} into the product of three matrices:

$$\mathbf{y} = \mathbf{U} \mathbf{\Lambda} \mathbf{V}^T \mathbf{x}$$

In this formulation, the matrix $\mathbf{\Lambda}$ is an M by M diagonal matrix of singular values organized in descending order, and \mathbf{V} is an M by M matrix with the corresponding orthonormalized eigenvectors of $\mathbf{A}^T \mathbf{A}$ as columns. Operating on the above with \mathbf{U}^T yields

$$(\mathbf{U}^T \mathbf{y}) = \boldsymbol{\beta} = \mathbf{\Lambda} (\mathbf{V}^T \mathbf{x}),$$

an expression relating linear combinations of the observations to linear combinations of the Schmidt coefficients that are linearly independent. Solutions may be constructed by summation over the eigenvectors (\mathbf{v}_i) associated with a subset k of the largest singular values, λ_i ,

$$\mathbf{x} = \sum_{i=1}^k \left(\frac{\beta_i}{\lambda_i} \right) \mathbf{v}_i$$

omitting parameter vectors associated with small or zero eigenvalues that have little or no expression in the available data. The omitted eigenvectors represent the model non-uniqueness, as they are combinations of the Schmidt coefficients that may be added to or subtracted from a solution vector without measurable effect on the observations. The extent to which an original parameter (Schmidt coefficient) is estimated is provided by the associated resolution matrix element, $R_{i,i}$, as described in prior work (e.g., Connerney, 1981; Connerney et al., 1998, 2018). Only well-resolved parameters are meaningfully constrained by the partial solution; those with $R_{i,i} \ll 1$ reveal covariability with other parameters that cannot be reasonably constrained.

3. Observations

Juno's magnetometer investigation (MAG) measures the magnetic field at 64 samples/s with a vector accuracy of ~ 1 part in 10^4 (Connerney et al., 2017) using boom-mounted fluxgate magnetometers at ~ 10 and ~ 12 m from the center of the spacecraft. The magnetometer boom extends from one of Juno's three solar arrays. Accurate attitude information is provided by a pair of MAG investigation star cameras located with each sensor (Connerney et al., 2017) whenever the star camera's field of view (FOV) is not obscured. A change in the mission plan from 14-day orbits to 53-day orbits necessitated use of an additional attitude sensor (spacecraft Stellar Reference Unit, or SRU) in combination with the MAG investigation's star cameras to provide continuity of attitude solutions. A comparison of the MAG investigation's attitude solutions with those of the spacecraft's SRU allows us to model,

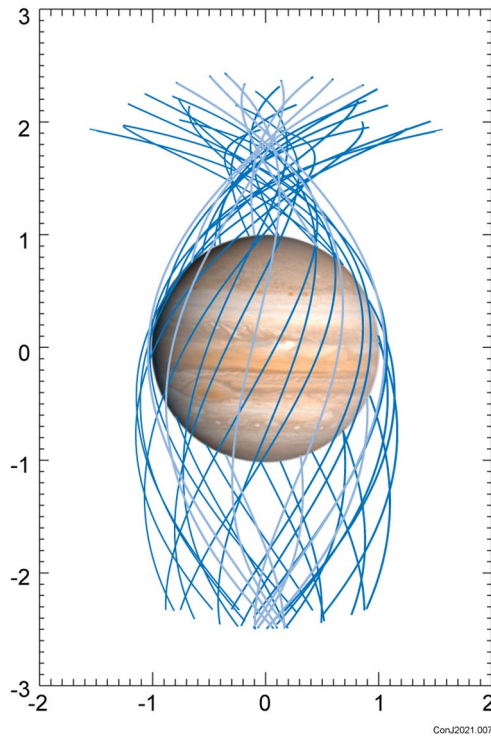


Figure 1. Juno's global mapping coverage after the 33 Prime Mission orbits. Juno's trajectory within $2.5 R_J$ radial distance is shown in projection on a plane containing Jupiter's spin axis and rotating with Jupiter. Orbits are separated by $\sim 11^\circ$ System III longitude where they cross the Jovigraphic equator. The first 8 orbital segments at $\sim 45^\circ$ separation that provided observations for the JRM09 model are rendered in a lighter shade of blue.

and correct for, slight attitude disturbances ($\lesssim 0.1^\circ$) experienced during peri-Jove resulting from heating of the solar array due to Jupiter shine (Herceg et al., 2020).

Observations of the vector magnetic field acquired within $2.5 R_J$ of Jupiter during the 33 orbits of the prime mission (Figure 1) were used to characterize Jupiter's planetary magnetic field. The measured magnetic field along Juno's trajectory within $2.5 R_J$ ranges from ~ 0.3 G to ~ 14.3 G, with a large variation in the maximum field experienced during a PJ pass depending primarily on the PJ longitude. The end members of this group are PJ13, crossing the equator at 29.3° System III(1965) longitude, which experienced a maximum field magnitude of just 3.20 G, and PJ29, crossing the equator at 175.8° System III(1965) longitude, with a maximum field magnitude of 14.31 G. The System III(1965) longitude system is a west longitude system as adopted by the International Astronomical Union (Seidelmann & Divine, 1977). Juno began orbital observations with a latitude at PJ01 just north of the equator (3.8°), and PJ latitude progresses northward by about 1° per orbit, reaching 28.8° by PJ33. Orbital inclination was very close to the pole (within 3°) for the first 8 orbits and subsequently relaxed (within 15°) for the remainder of the Prime Mission. As Juno continues in Extended Mission, it will continue to sample the field at progressively lower altitudes over the extended region of high field strengths at northern mid-latitudes.

Juno is a spinning spacecraft with a spin period of 30 s. Our inversions used 30-s (spin period) averages of the magnetic field rendered in a Jupiter-centered, spherical coordinate system, sufficient to follow variations in the field and useful in reducing any residual spin modulation arising from calibration errors or Eddy current correction errors (Kotsiaros et al., 2020). The Eddy current corrections are as large as ~ 2 parts in 10^4 , depending on the orientation of the field relative to the sc spin axis (Kotsiaros et al., 2020); calibration errors are comparable in magnitude. The large dynamic range of operation of the fluxgate is accommodated by six analog dynamic ranges, with a capability of ± 16 G per sensor coordinate axis in the uppermost dynamic range

(Connerney et al., 2017). The instrument ranges up and down autonomously in response to changes in the ambient magnetic field, preserving accuracy of measurement with the dedicated 16-bit analog to digital converter on each axis. Each observation is scaled to a proxy for the accuracy of measurement in each of the dynamic ranges, taken as the 16-bit quantization uncertainty ΔQ associated with the current dynamic range. Each perijove segment within $2.5 R_J$ begins and ends with observations acquired with $\Delta Q = 3.125$ nT, increasing to 12.5 nT, and (often) 50. nT, depending on the maximum field experienced during transit. Magnetospheric "noise," based on experience with prior, more distant flybys, is typically a few nT in magnitude (e.g., Connerney et al., 1982).

4. Results

The JRM09 model used a spherical harmonic model with a maximum degree and order, N_{\max} , of 20, sufficient to minimize the model residuals along the 8 orbit segments available at that time. A partial solution to that linear system (including 264 of 440 possible eigenvectors) yielded well resolved coefficients through degree 10. Here, with more complete global coverage, we adopt a model representation with a maximum degree and order $N_{\max} = 30$ and seek to minimize the residuals along the 32 orbit segments upon completion of the global map with $\sim 11^\circ$ separation between orbits, measured at descending equator crossing. All inversions approximate the external field with a degree 1 external spherical harmonic, equivalent to a uniform field, which is sufficient near the origin; such models are abbreviated as I30E1 models to identify the internal and external expansion limits. In a partial solution, the choice of N_{\max} is less important than the number of eigenvectors included in the solution, if it is large enough to follow the spatial variation of the field at close-in radial distances.

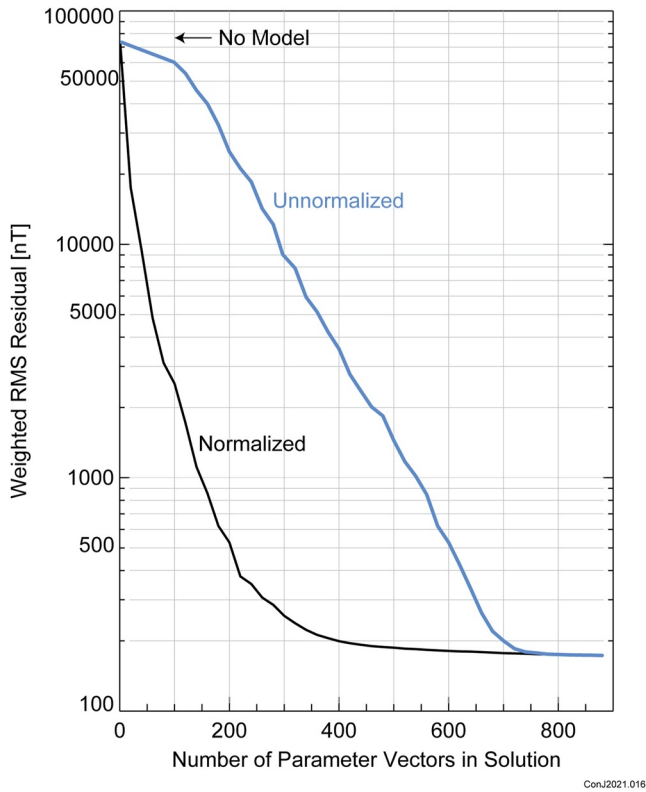


Figure 2. Improvement in goodness of fit, represented by weighted root-mean-square (RMS) residual, as a function of the number of eigenvectors included in the solution, fitting an I30E1 spherical harmonic model with unnormalized (blue) versus normalized (black) parameters.

A model solution is constructed by summation over the independent eigenvectors of parameter space, progressively including a larger number of parameter vectors until minimal improvement in the fit is afforded by additional eigenvectors. As more eigenvectors are included in the solution, model parameter resolution improves, and additional terms (Schmidt coefficients) are included among the set of “well resolved” coefficients. The singular value decomposition (SVD), and model solution, simultaneously minimizes the misfit to the data and the magnitude of the parameter vector and therefore depends on parameter normalization. The JRM09 model used a parameter scaling consistent with an expectation of equal amplitudes by harmonic degree on a core radius of $0.85 R_j$, implemented by parameter scaling via r_c^{n-1} where $r_c = 0.85$ and n is harmonic degree. We will begin by constructing a partial solution without parameter scaling (equivalently, $r_c = 1 R_j$) to demonstrate that there is indeed a natural choice for r_c and to illustrate, by analogy to the spectrum of the Earth’s magnetic field, the reach of the current distribution of orbits.

An I30E1 model constructed *without* parameter weighting, using 780 of the 963 possible eigenvectors (includes the three external field coefficients) fits the observations with a weighted RMS residual (174 nT) that cannot be meaningfully reduced by inclusion of additional eigenvectors (Figure 2). This model is sufficient to resolve well ($R_{nn} > 0.90$; see Supporting Information S1) almost all spherical harmonic coefficients through degree and order 10 (only). This does not extend the list of well-resolved Schmidt coefficients beyond that found earlier, with the model solution of JRM09, which used parameter weighting ($r_c = 0.85$) to reduce covariability of low degree terms with those of higher degree.

A Lowes’ plot of the magnetic spectrum (Lowes, 1974) of this model is shown in Figure 3, along with that of the Earth for comparison. The magnetic spectrum R_n displays the magnetic energy on the planet’s (spherical) surface contributed by each spherical harmonic degree; for the Earth model field, we used terms up to degree 30 from NOAA’s enhanced magnetic model

(emm2017) provided by the National Geophysical Data Center (Chulliat et al., 2015). The linear fit to the magnetic spectrum is most often performed omitting the dipole and quadrupole terms (e.g., Lowes, 1974). Jupiter’s magnetic field, and Saturn’s, both evidence a relatively weak quadrupole as well (Connerney, 1993, 2015) leading to the supposition that the “quadrupole deficit” is a common feature of dynamo generation.

The magnetic spectrum may be calculated on any spherical surface exterior to the dynamo via

$$R_n(r, r \geq r_c) = R_n \left(\frac{a}{r} \right)^{2n+4}$$

A linear relationship among the terms of R_n implies a core radius r_c at which harmonics of all degrees contribute equally to the field. This is sometimes called the “Lowes radius.” The Earth’s magnetic spectrum (degrees 3 through 14) is fit well with a magnetic core radius ($0.537 \pm 0.014 r_e$) very close to that of the seismically determined fluid core (Cain et al., 1989; Langel & Estes, 1982; Langlais et al., 2014; Lowes, 1974; Tsang & Jones, 2020), leading to the conclusion that the dynamo core radius may be determined by such a fit. It is at least plausible that a magnetic dynamo produces a field with a comparable distribution of magnetic energy over spatial scales associated with harmonic degree n (Backus et al., 1996). For the Earth, the break in the spectrum near $n = 14$ is identified with a transition from the field associated with the dynamo at depth to one ($n > 14$) associated with a random distribution of sources (crustal magnetization) near the surface (Cain et al., 1989; Langel & Estes, 1982; Lowes, 1974). By analogy with Earth, the Jupiter magnetic spectrum might be interpreted as that due to a dynamo with core radius of $0.806 \pm 0.006 r_j$ transitioning at high degree to a spectrum resulting from random noise contributions.

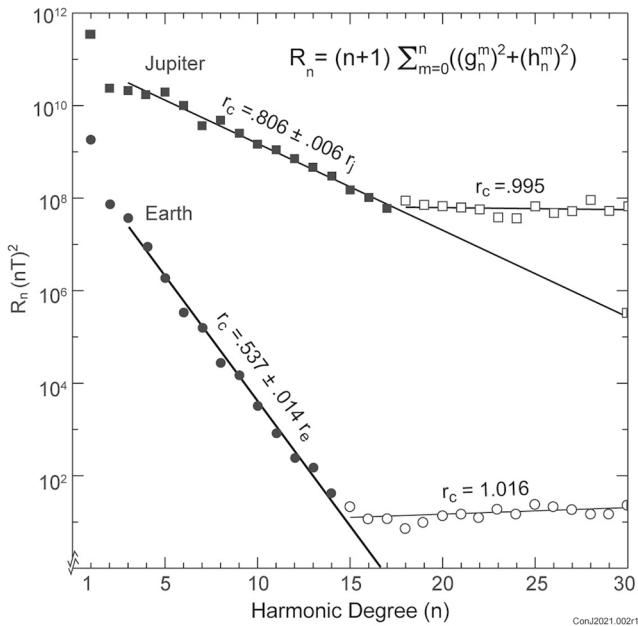


Figure 3. Lowes' plot of the magnetic spectrum for Earth (circles) and a model fit to Juno observations (squares) without parameter normalization. Filled symbols are associated with the field of the dynamo and well fit (omitting $n = 1, 2$) by a linear progression in harmonic degree.

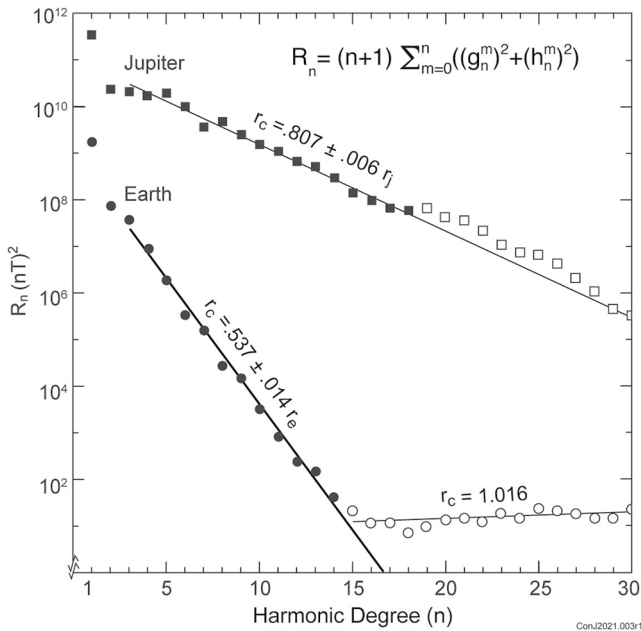


Figure 4. Lowes' plot of the magnetic spectrum for Earth (circles) and a model fit to Juno observations (squares) with parameter normalization. Filled symbols are associated with the field of the Jovian dynamo and are well fit (omitting $n = 1, 2$) by a linear progression in harmonic degree through degree 18.

The linear trend identified for Jupiter among degrees 3–17 in Figure 3 suggests a partial solution with parameter scaling via r_c^{n-1} where $r_c = 0.8$ and n is harmonic degree. Implicit in this choice of parameter normalization is the expectation that the trend identified among the lower degree terms (3–17) extends to higher degree. A second I30E1 inversion was performed with parameter scaling appropriate to the expectation of equal amplitudes by degree at $r_c = 0.8 R_J$, leading to a solution using 620 eigenvectors (of 963 possible) with an RMS residual of 179. nT, a reasonable compromise between model parameter resolution and goodness of fit. This model (“JRM33,” Juno reference model through perijove 33) has reasonably well resolved Schmidt coefficients through degree and order 13, with useful information extending through degree and order 18. The parameter normalization has the effect of suppressing covariability with higher degree terms and improves model parameter resolution to higher degree relative to a model construction with $R_c = 1 R_J$. As is apparent in Figure 2, construction of solutions with this parameter normalization proceeds with eigenvectors that are much more efficient in reducing the RMS residual, compared to the prior exercise. Figure 4 shows the Lowes magnetic spectrum for this model, with a Lowes' radius fit to degrees 3–18 of $r_c = 0.807 \pm 0.006 r_J$, again compared with that of Earth.

The subset of Schmidt coefficients through degree and order 18 is referred hereafter as the “JRM33” model field. We provide the entire model solution, that is, all 963 parameters, including the 3 external Schmidt coefficients, for reference but caution that only well resolved coefficients (those with resolution matrix diagonal elements approaching 1.0) are meaningfully constrained. The model parameters are listed in machine-readable format, along with the corresponding resolution matrix element, and a Schmidt coefficient identifier in the online supplement. The degree 1 coefficients of the JRM33 model describe a dipole with moment $M = 4.177$ G, offset from the rotation axis by $\theta_d = 10.25^\circ$ towards System III longitude of $\phi_d = 196.38^\circ$. Differences with the previous JRM09 model dipole ($\Delta M = 0.007$ G, $\Delta\theta_d = 0.06^\circ$, $\Delta\phi_d = 0.23^\circ$) are slight. The difference in longitude of the dipole will be addressed in the discussion section with reference to uncertainty in the rotation period of Jupiter.

The field magnitude computed on the surface of a dynamically flattened (1/15.4) Jupiter is illustrated with the aid of Figure 5, a rectangular latitude-longitude plot, and Figure 6, presenting orthographic projections of the field at the poles. Each also includes the computed path of the Io Flux Tube footprint compared with recent IFT footprint observations obtained by Juno's JIRAM investigation (Adriani et al., 2017; Mura et al., 2018). The JIRAM observations, acquired from Juno's unique polar vantage point, offer a more accurate determination of the latitude and longitude of the IFT footprints than that obtained from Hubble Space Telescope (HST) imagery (Bonfond et al., 2017), particularly along the path near the pole, difficult to observe from an equatorial vantage point. This comparison serves as an independent check of the geometry of the field, since IFT observations were not used to constrain the field model (unlike the VIP4 model, which included the IFT footprint locations as a constraint). A listing of the modeled satellite footprints for Amalthea, Io, Europa, and Ganymede, computed using the JRM33 model and the magnetodisc model of Connerney et al. (2020), is provided in the online supplement.

The magnetic field magnitude computed at Jupiter's surface varies from a minimum of just under 2 Gauss to a maximum of almost 22 Gauss. Surface

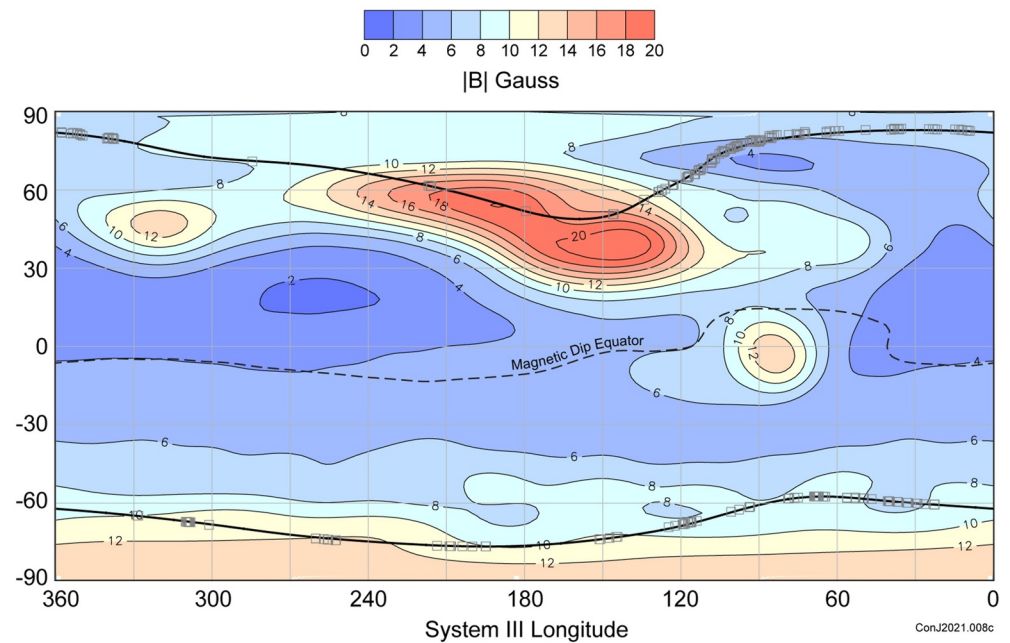


Figure 5. Contours of the magnetic field magnitude (Gauss) on the dynamically flattened (1/15.4) surface of Jupiter in rectangular latitude-longitude projection. Io Flux Tube (IFT) footprint observations (squares) obtained by the Jovian Auroral Infrared Auroral Mapper (Adriani et al., 2017) are compared to the path of the IFT (black curve) computed from the JRM33 model. The JRM33 magnetic dip equator is shown with a dashed line.

magnetic field strengths along the IFT footprint approach a maximum of 20 Gauss in the north (near 190° System III longitude) and 12 Gauss in the south (near 240° System III), well more than needed to explain Io-related radio observations originating from the IFT footprint (e.g., Genova & Aubier, 1985; Hess et al., 2011; Martos et al., 2020).

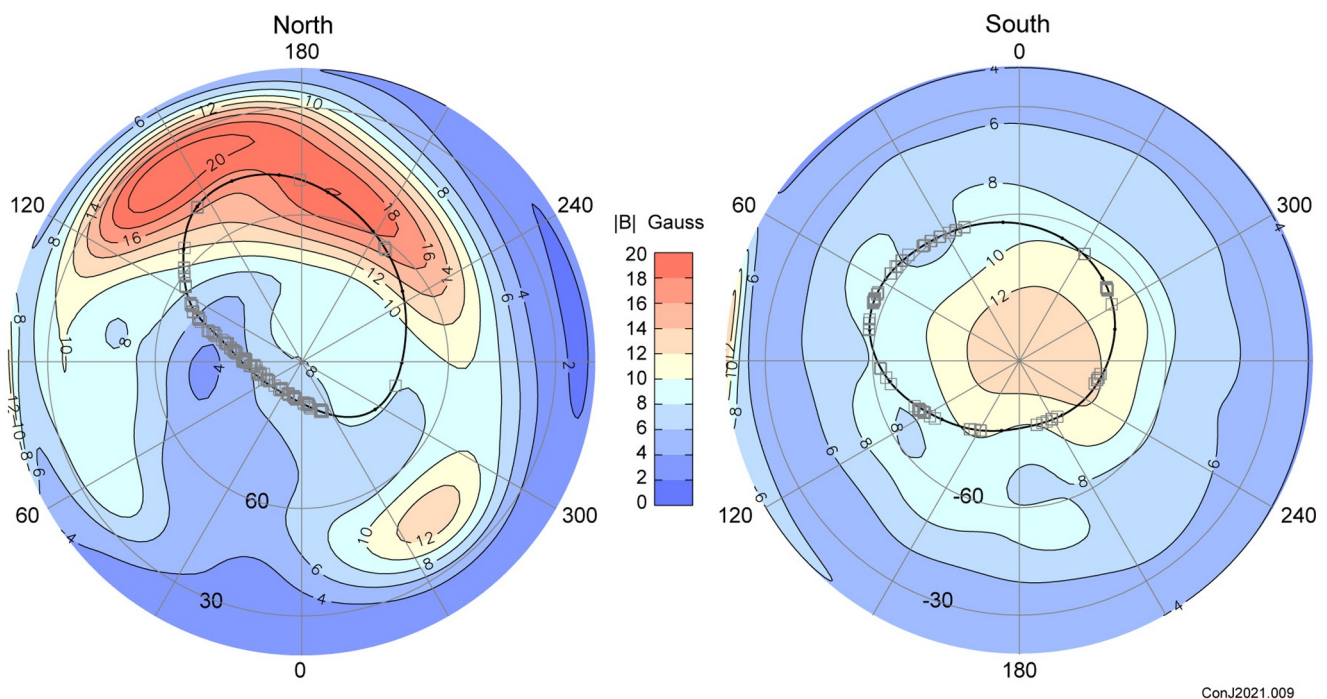


Figure 6. Same as Figure 5 but in orthographic polar projection.

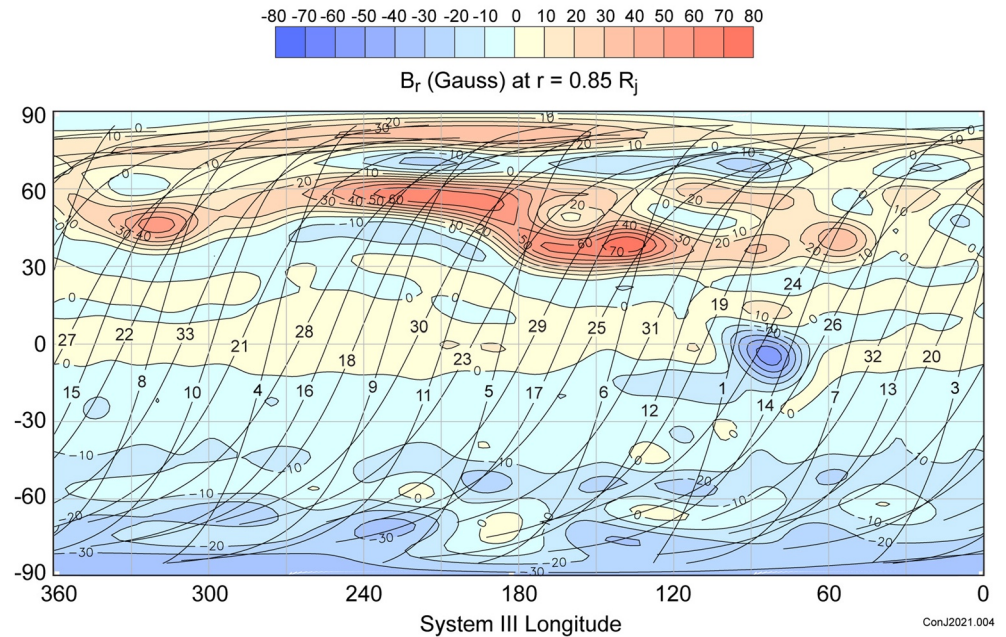


Figure 7. Contours of the radial magnetic field (Gauss) on the dynamically flattened surface with equatorial radius $r_c = 0.85 R_j$ in rectangular latitude-longitude projection. The sub-spacecraft latitude and longitude for the 32 numbered Juno orbits (PIs 1, 3–33) used in modeling the field is also shown for spacecraft radial distances $<2.5 R_j$. An orthographic projection of this figure is provided in Supporting Information S1.

The degree 18 representation of the field brings into sharper focus the extraordinary hemispheric difference Jupiter's magnetic field (Connerney et al., 2017; Moore et al., 2018) and a peculiar isolated equatorial patch of intense magnetic field near 90 degrees System III west longitude. This feature, referred to as the Great Blue Spot (GBS), is more clearly identified in a contour map of the radial field at $0.85 R_j$ presented in Figure 7 (to be compared with a similar figure in Connerney et al., 2017, using the JRM09 model). Also noteworthy is a north polar band of reversed flux extending most of the way around the pole at about 70° north latitude, possibly a circumpolar band of reversed flux. There is a suggestion of the presence of a similar band of reversed flux about the southern pole at comparable southern latitude. The presence of a north polar anomaly was inferred previously to explain HST observations of the IFT footprint and aurora (Grodent et al., 2008). We have chosen to use coefficients through degree 18, in this presentation, even though those beyond degree 13 are not well resolved, recognizing the small spatial scale of notable features. As a result, some minor artifacts are to be expected in a contour map drawn for projections at radial distances beneath the surface. Figure 8 compares the radial magnetic field in Mollweide projection at for radial distances (1.0, 0.95, 0.90, and $0.85 R_j$).

5. Discussion

The magnetic spectrum of the JRM33 model (Figure 4) reveals a magnetic field remarkably similar to Earth's, albeit with an apparent dynamo core radius much larger than Earth's, if we accept the presumption that the Lowes plot identifies the dynamo core radius (Elphic & Russell, 1978; Langel & Estes, 1982; Lowes, 1974; Tsang & Jones, 2020). This similarity was recognized decades ago (Connerney, 1993; Stevenson, 1983) based on a comparison of dipole tilt and the relative magnitude of the first few harmonic degrees and is strengthened considerably by extension to high degree. Nevertheless, the magnitude of Jupiter's field dwarfs Earth's by orders of magnitude and the hemispheric dichotomy of Jupiter's field sets it apart from Earth (Moore et al., 2018). Jupiter's dipole moment is some $\sim 20,000$ times that of Earth's, as might be expected of a convection-driven planetary dynamo driven by basal heating (Olson & Christensen, 2006). In contrast, the hemispheric dichotomy of the field was a major surprise, unanticipated by dynamo simulations (Moore et al., 2018).

The linear fit to Jupiter's magnetic spectrum with $r_c = 0.807 \pm 0.006 R_j$ suggests dynamo generation of the field near the outer extremity of the convective metallic hydrogen region that is common to all models of the interior

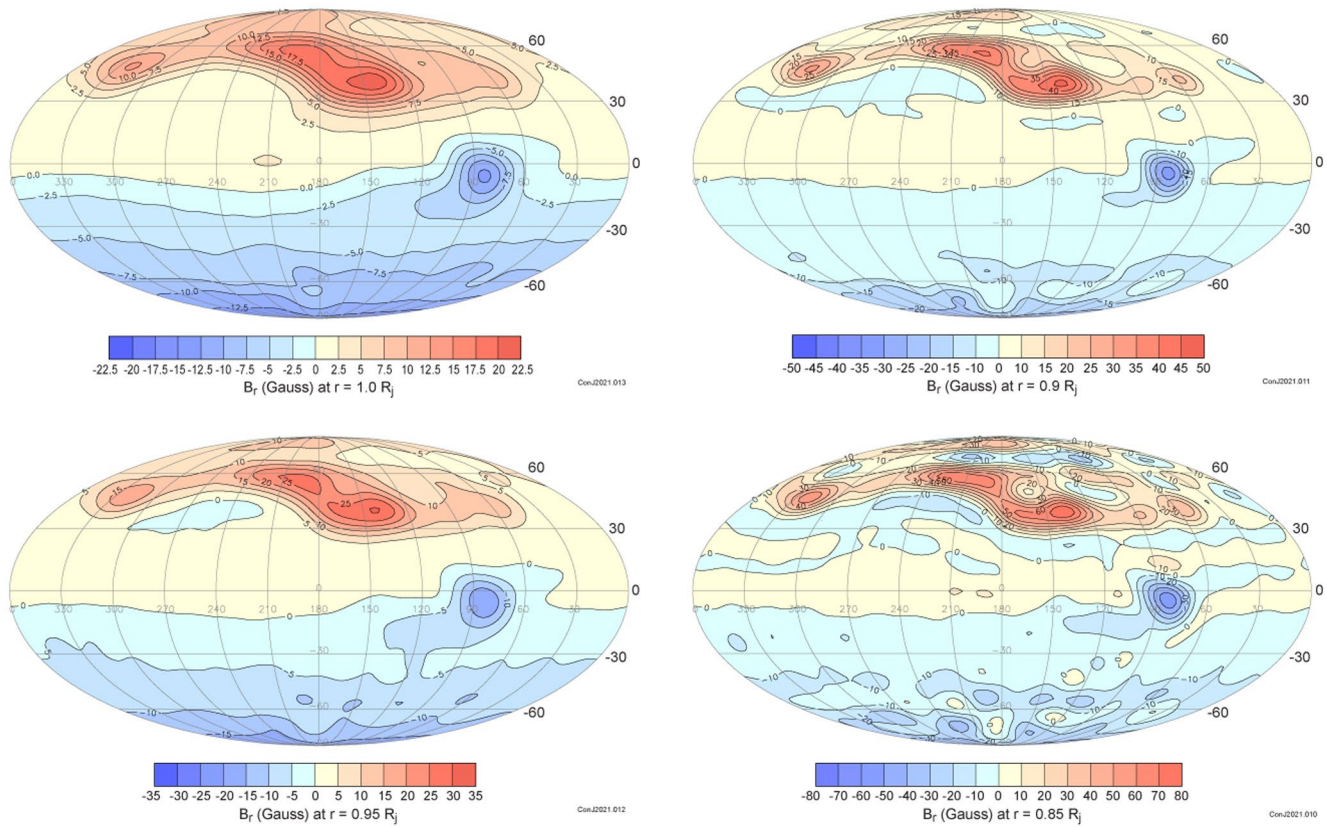


Figure 8. Contours of the radial magnetic field (Gauss) on dynamically flattened surfaces with equatorial radii $r_c = [1.0, 0.95, 0.90, \text{ and } 0.85] R_j$ in Mollweide projection. Contour intervals are chosen to span 7–9 contour levels in the northern hemisphere.

(Guillot et al., 2004; Nellis, 2000; Stevenson, 1983) and just beneath the presumably non-convective helium rain layer. Laboratory shock experiments indicate that hydrogen transitions to a metallic fluid at pressures in excess of ~ 140 GPa (1.4 Mbar) at temperatures relevant to Jupiter's interior (Nellis et al., 1999; Weir et al., 1996). Precisely where this occurs in Jupiter's interior is not known, but estimates place the transition to metallic hydrogen between $0.8 R_j$ (Stevenson, 1983) and $0.9 R_j$ (French et al., 2012; Nellis, 2000). Since the Lowes radius now appears to be well determined, one might suggest that it locates, approximately, the outer boundary of convective metallic hydrogen at or near $0.81 R_j$ in Jupiter's interior. Above this presumed dynamo core radius, interior models (Guillot et al., 2004; Stevenson, 2020) place a shell of non-convective metallic hydrogen, stabilized by the precipitation of helium droplets (“helium rain”) due to the immiscibility of helium and hydrogen (Salpeter, 1973; Smoluchowski, 1967). Gastine and Wicht (2021) place the base of the stably stratified layer between 0.82 and $0.86 R_j$, the lower figure just beyond the Lowes radius of the JRM33 model. Their most recent dynamo model does produce a Lowes radius much like that shown here, aside from a too-large dipole term. There is not universal agreement on the presence of a helium rain layer within Jupiter's interior, but recent laboratory experiments on hydrogen-helium mixtures at high pressure and temperature (Brygoo et al., 2021) suggest such region within Jupiter (0.68 – $0.84 R_j$), perhaps much too broad a region, if non-convecting, to support dynamo activity to $0.81 R_j$.

The concept of a dynamo core radius is less well defined as applied to Jupiter, in contrast to Earth, where the core is very precisely located by a profound discontinuity in many material properties (Guillot et al., 2004). Jupiter's interior lacks such an abrupt transition that might ground a definition of a dynamo core radius related to a local property. The phase transition from molecular to metallic hydrogen is thought to be continuous and as a result the electrical conductivity varies smoothly with radius, with no abrupt barrier to dynamo action (Tsang & Jones, 2020). Dynamo action is also possible at depth, locally, within the molecular hydrogen envelope above the transition to metallic hydrogen (French et al., 2012; Smoluchowski, 1975), and as such may contribute to the magnetic spectrum at high degree (beyond the reach of our current modeling). However, the magnetic Reynolds

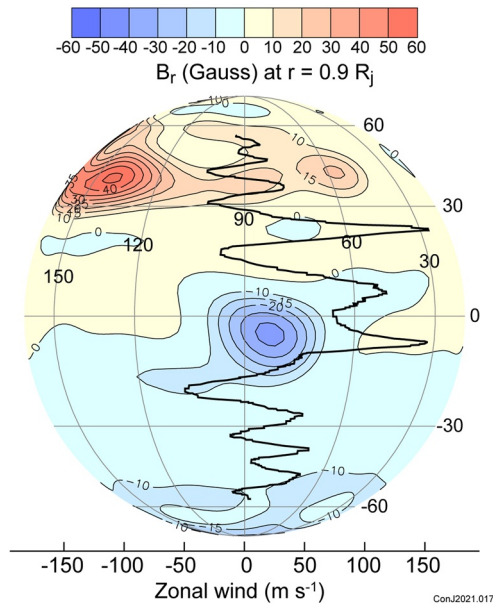


Figure 9. Contours of the radial component of the JRM33 model magnetic field using terms to degree 18 to calculate the field on a surface at $0.9 R_j$ radius, compared to the variation in zonal wind velocities observed at the surface (Simon et al., 2015).

number in the convective molecular hydrogen envelope may be too small to sustain dynamo action (Gastine & Wicht, 2021).

The molecular hydrogen layer above the metallic hydrogen is electrically conductive enough at depth (French et al., 2012; Nellis et al., 1996) to grip magnetic field lines, even if dynamo action is not possible; deep zonal winds extending to depths of a few thousand km (Guillot et al., 2018; Kaspi et al., 2018) may translate and/or shear the field, leading to an observable secular variation over a relatively short interval of time (Moore et al., 2019). Moore et al. (2019) compared earlier Pioneer, Voyager, and Ulysses flyby observations of Jupiter's magnetic field with the JRM09 model and demonstrated that the field has measurably changed over the four and a half decades prior to Juno's orbit insertion. The secular variation was found to be consistent with advection of the field by deep zonal winds, scaled from the zonal wind velocities measured at the cloudtops (Moore et al., 2019). The contours of the radial field shown in Figure 8 are suggestive of radial flux being transported to the west on the southern flank of the GBS and to the east on the northern flank, consistent with the zonal wind pattern observed at the surface (Porco et al., 2003; Simon et al., 2015). In Figure 9 we show an orthographic projection of the radial field contoured on a surface at $0.9 R_j$ and compare that with the variation in zonal wind velocity observed at the surface (Simon et al., 2015). It is important to note that Jovimagnetic secular variation detected thus far is a localized phenomenon, in contrast to the dipole (low degree) variation that has been the subject of prior speculation (Connerney & Acuña, 1982; Ridley & Holme, 2016; Russell & Dougherty, 2010; Yu et al., 2009).

It is also of interest to examine the differences between the JRM33 and JRM09 models. As noted previously, the differences in the dipole coefficients are small, $\Delta g_1^0 = 0.18\%$, $\Delta g_1^1 = 0.26\%$ and $\Delta h_1^1 = 1.7\%$. The JRM33 dipole longitude ($196.38^\circ \lambda_{III}$) is $\sim 0.2^\circ$ west of the JRM09 dipole longitude ($196.6^\circ \lambda_{III}$), but the difference is within the estimated uncertainty of the rotation period ($9\text{h } 55\text{m } 29.711 \pm 0.04\text{s}$) upon which system III (1965) is based (Seidelmann & Divine, 1977). In this system Jupiter rotates by $810.536 \pm 0.0009^\circ/\text{day}$; in the 1.75 years between the JRM33 epoch (2019) and the JRM09 epoch (2017.25) the uncertainty in longitude equates to 0.57° . However, if we compare the JRM33 dipole longitude with that obtained from the Voyager flyby in 1979 (V1_17ev model of Connerney et al., 1982) and the Ulysses flybys in 1992 (Uly_17ev model of Connerney et al., 1996) we can infer an average coordinate system drift rate of $\sim 0.09^\circ/\text{yr}$, essentially the same as that found by Moore et al. (2019) and Ridley and Holme (2016), and well within the estimated uncertainty in System III rotation rate.

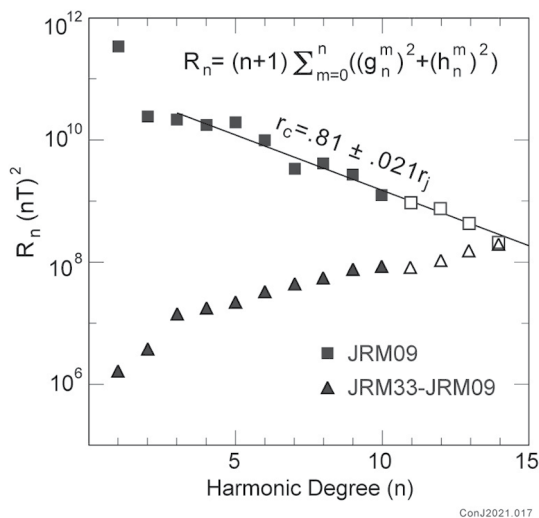


Figure 10. Lowes' plot of the magnetic spectrum of the JRM09 model compared with that of the difference (JRM33 – JRM09) through degree 14. Filled symbols are used to identify spectrum estimates (and differences) computed using the well resolved JRM09 coefficients (through degree 10). The Lowes radius for the JRM09 model is fit using degrees 3–10.

We compare differences between the JRM09 and JRM33 models using a Lowes plot of the magnetic spectrum. Figure 10 compares the difference in magnetic spectrum between JRM09 and JRM33 by plotting the JRM09 spectrum and the spectrum of the difference (JRM33 – JRM09) so that a measure of the minor differences is visible. We have extended the comparison beyond JRM09's well resolved degree 10 representation (filled symbols) as this plot demonstrates that a case can be made for a meaningful comparison of these two models to perhaps degree 13. At low degree the differences are quite small ($<0.001\%$) growing approximately linearly with degree until by degree 14 the difference catches up with the spectrum.

We also compare the two models by computing the difference in radial field on the (flattened ellipsoid) surface of Jupiter. To do so, we must choose a spherical harmonic expansion to common degree (n_{max}) and have elected to use $n_{\text{max}} = 13$ as a compromise between model parameter resolution afforded

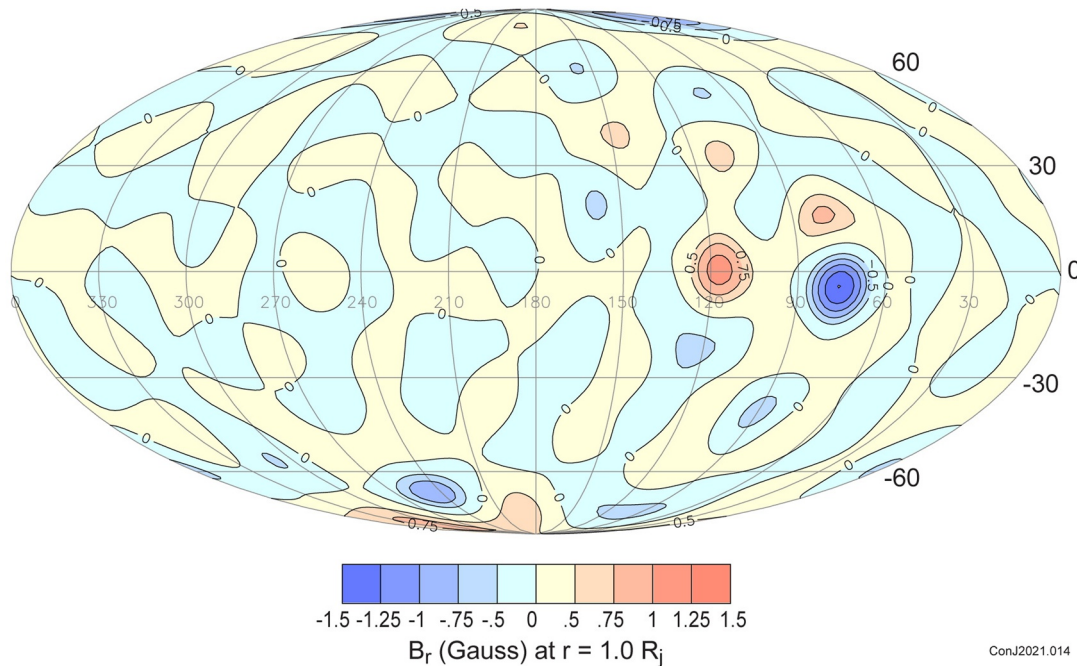


Figure 11. Contours of the radial component of the magnetic field obtained by subtracting the JRM09 model through degree 13 (epoch 2017.25) from the JRM33 model through degree 13 (epoch 2019.0), assigning each an epoch corresponding to the center of the data collection interval. The degree 13 expression of the difference is large near the Great Blue Spot and small elsewhere, but for the region near the south pole less well sampled by Juno's trajectory.

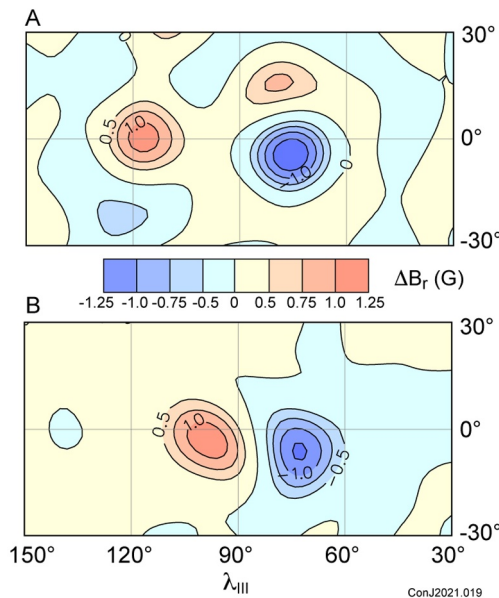


Figure 12. Comparison of the secular variation observed between the two model epochs (2017.25 and 2019) with that computed from the JRM33 model assuming eastward drift of the Great Blue Spot. Observed secular variation (panel A) computed by subtracting the radial field of the JRM09 model (extended to degree 13) from that of the JRM33 model through degree 13. Modeled secular variation of radial field (panel B) computed by subtracting a shifted (~2,500 km) JRM33 model radial field from the JRM33 model radial field.

by the JRM09 and JRM33 models (Supporting Information S1). The difference between the radial field calculated using JRM33 through degree 13 and that calculated using JRM09 (extended through degree 13) is displayed across the surface (Mollweide projection) in Figure 11. The degree 13 expression of the difference is large near the Great Blue Spot and small elsewhere, but for the region near the south pole. Juno's trajectory passes over the southern pole at much larger radial distances (see Figure 1) due to the steady northward progression of its periapsis, and as a result the field is less well constrained near the south pole.

The difference is greatest on the flanks of the GBS where the spatial gradient of the field is largest, and both wind velocity (eastward at $\sim 100 \text{ ms}^{-1}$) and wind shear are great as measured on the surface (Porco et al., 2003; Simon et al., 2015). This variation of the magnetic field (secular variation) is as predicted by Moore et al. (2019) based on a comparison between the JRM09 model and data obtained three and four decades ago during the Voyager and Ulysses flybys. The excess radial field on the flanks of the GBS appears to be ~ 0.5 Gauss in magnitude, which, if acquired over the nearly 2 years between model epochs, equates to $\sim 0.28 \text{ Gyr}^{-1}$. This is comparable to Moore et al.'s (2019) estimate of 0.15 Gyr^{-1} . Note that the lack of a similar feature associated with the mid northern latitude (positive) flux band, which also exhibits large horizontal gradients in the field, rules out a simple coordinate system drift (due to rotation period inaccuracy) as an alternative explanation.

The difference in radial field between the two epochs can be largely accounted for by the transport of the GBS eastward by about 2 degrees in longitude, or $\sim 2,500 \text{ km}$, in 1.75 years. Figure 12 compares the change in radial field observed (JRM33 model – JRM09 model, through degree 13) with that obtained by subtracting a shifted (west by 2°) JRM33 radial field (through

degree 18) from the JRM33 model radial field. A very similar plot is obtained if JRM33 is truncated at degree 13 as well. If we assume frozen flux, the implied fluid velocity required to transport the field during the time between epochs is $\sim 0.04 \text{ ms}^{-1}$ at a depth where the electrical conductivity is large enough to satisfy the frozen flux assumption. This occurs where the timescale for transport of the field ($v_c L$, where v_c is the fluid velocity, L a characteristic length scale) exceeds by a factor the timescale for diffusion out of the conductor (λ_m , magnetic diffusivity, inversely proportional to the electrical conductivity). The ratio ($R_m = v_c L / \lambda_m$) is the familiar magnetic Reynolds number of dynamo theory when a convective fluid velocity is chosen for v_c . With $v_c = 0.04 \text{ ms}^{-1}$, and $L = 200 \text{ km}$, suggested by the electrical conductivity scale height (Cao & Stevenson, 2017) at depth, an $R_m \sim 10$ requires an electrical conductivity of $\sim 1000 \text{ S/m}$, which is found at $0.95 R_j$ (Cao & Stevenson, 2017; French et al., 2012). This compares well with that (0.0375 ms^{-1}) found by Moore et al. (2019) at $0.95 R_j$ radial distance, a depth of $\sim 3,500 \text{ km}$ below the surface. The comparison of the two Juno magnetic field models confirms, both qualitatively and quantitatively, the inferences drawn by Moore et al. (2019) from their retrospective analysis of earlier flybys using the JRM09 model as a reference.

Before we conclude, two observations from Figures 5 and 6 deserve mention. The first concerns the distribution of IFT footprint observations obtained by the JIRAM investigation. The IFT footprint is observed in JIRAM's L-band ($3.3\text{--}3.6 \mu\text{m}$) infrared imagery which is dominated by multiple prominent H_3^+ emission lines. These emissions are thermally excited and provide a measurement of upper atmospheric temperature and thereby a measure of energy deposition at the foot of the IFT. The footprint is most often observed by JIRAM in the north polar region in areas of relatively weak surface magnetic field strength, indicating that the strength of the Io interaction is greatest where Jupiter's surface magnetic field is weakest. This trend was noted when the first IFT footprint observations were reported (Connerney et al., 1993), also in the IR. In the ultraviolet (UV) the IFT footprint is observed at all longitudes, including where surface magnetic field is strong (Bonfond et al., 2013; Clarke et al., 2002) and the southern footprint is much brighter (Bonfond et al., 2013) than that in the north. The IR and UV IFT emissions originate at different atmospheric densities, the IR emissions tracking energy deposition, and the UV tracking particle precipitation, at different altitudes; one should not assume they behave in tandem.

The second observation from Figure 5 concerns the excursion of the magnetic dip equator in the vicinity of the GBS. The path of the magnetic equator was detected in H_3^+ imagery (Stallard et al., 2018) acquired at the Infrared Telescope Facility (IRTF), closely matching that calculated using the JRM09 model (Connerney et al., 2017) as well as that calculated here using JRM33. But the anomaly we now call the GBS may have been detected decades ago, in the linear polarization of radio emissions (Conway & Stannard, 1972) at wavelengths of 6, 11, and 21 cm. They proposed the presence of a magnetic anomaly near the equator at $\sim 220^\circ \lambda_{III}$ (1957) to explain the non-sinusoidal variation in position angle of linear polarization with central meridian longitude. The 1957 System III coordinate system uses a different rotation rate and definition of the zero longitude (Seidelmann & Divine, 1977); translating to System III(1965) places the longitude of their proposed anomaly at $56^\circ \lambda_{III}$ (1965), near the excursion in the magnetic equator associated with the GBS. Conway and Stannard's proposed magnetic anomaly is an *equatorial* anomaly, distinct from the high latitude magnetic anomaly (or anomalies) invoked to explain magnetospheric phenomena (Dessler & Hill, 1975, 1979) and the path of auroral emissions (Grodent et al., 2008).

6. Conclusions

We present a degree 18 spherical harmonic model of Jupiter's planetary magnetic field, offering the most detailed view of a planetary dynamo ever obtained. The Earth's magnetic field is well characterized to very high degree and order, but our view of the dynamo is obscured by crustal magnetization at or beyond degree ~ 14 . The Jovian magnetic field has features with spatial scale challenging the reach of the Prime Mission's 33 orbits, with adjacent orbits separated by $\sim 0.2 R_j$ where they cross the equator. If we take the linear fit to the Lowes spectrum ($0.807 R_j$) as an estimate of the dynamo core radius, our 32 orbits are about as far apart as they are above the outer boundary of the source. The Extended Mission plan puts orbits between the existing orbits to the extent possible, increasing global mapping coverage to provide ever greater spatial resolution of the field. A dedicated magnetic survey over the GBS is to be performed early in Extended Mission, during orbits 36–42, to characterize secular variation of the field associated with the GBS and perhaps the deep zonal flow that grips and transports the field over a remarkably short time (Moore et al., 2019).

The Lowes radius of the JRM33 model (at $0.81 R_J$) suggests dynamo generation in metallic hydrogen beneath a non-convective layer of metallic hydrogen stabilized by the precipitation of helium droplets (“helium rain”). The JRM33 model presented here, differenced with the JRM09 model based on Juno’s first 9 orbits, provides independent evidence of the secular variation of the field over a very limited (less than 5 years) time span. The secular variation appears in association with the GBS, as predicted by Moore et al. (2019), and is confined to a small region around the GBS. It may be explained in part by drift of the GBS analogous to that of the Great Red Spot (Simon et al., 2018) and by shear of the GBS (Moore et al., 2019) due to the variation in deep zonal winds with latitude. Secular variation of the field near the GBS provides independent evidence of the penetration of zonal winds to depths of thousands of km, where molecular hydrogen becomes sufficiently electrically conductive (Cao & Stevenson, 2017; Nellis et al., 1996) to modify the field via relative motion.

Conflict of Interest

The authors declare no conflicts of interest relevant to this study.

Data Availability Statement

Data supporting the conclusions are archived (Connerney, 2017) with the NASA Planetary Data System at <https://pds.nasa.gov> along with the model coefficients (“JRM33.mod”) listed in ASCII file format and also found among Supporting Information S1.

Acknowledgments

We thank the project and support staff at the Jet Propulsion Laboratory (JPL), Lockheed Martin, and the Southwest Research Institute (SWRI) for the design, implementation, and operation of the Juno spacecraft. The Jet Propulsion Laboratory, California Institute of Technology, under contract to the National Aeronautics and Space Administration (80NM0018D0004), manages the Juno mission for the principal Investigator, S. Bolton, of SWRI. We especially thank Monte Kaelberer, Ever Guandique, and Paul Romani at GSFC and Carol Ladd at the Space Research Corporation for expert support. K. Moore acknowledges financial support via the 51 Pegasi b Fellowship from the Heising-Simons Foundation. This research is supported by the Juno Project under NASA grant NN-M06AaA75c to SWRI, and NASA grant NNN12AA01C to JPL/Caltech. The Juno mission is part of the New Frontiers Program managed at NASA’s Marshall Space Flight Center in Huntsville, Alabama.

References

- Adriani, A., Filacchione, G., Di Iorio, T., Turrini, D., Noschese, R., Cicchetti, A., et al. (2017). JIRAM, the Jovian infrared auroral mapper. *Space Science Reviews*, 213, 393–446. <https://doi.org/10.1007/s11214-014-0094-y>
- Backus, G., Parker, R., & Constable, C. (1996). *Foundations of geomagnetism*. Cambridge University Press.
- Bolton, S. J., Adriani, A., Adumitroaie, V., Anderson, J., Atreya, S., et al. (2017). Jupiter’s interior and deep atmosphere: The first close polar pass with the Juno spacecraft. *Science*, 356, 821–825. <https://doi.org/10.1126/science.aal2108>
- Bolton, S. J., Lunine, J., Stevenson, D., Connerney, J. E. P., Levin, S., Owen, T. C., et al. (2017). The Juno mission. *Space Science Reviews*, 213, 5–37. <https://doi.org/10.1007/s11214-017-0429-6>
- Bonfond, B., Hess, S., Gerard, J.-C., Grodent, D., Radioti, A., Chantry, V., et al. (2013). Evolution of the Io footprint brightness I: Far-UV observations. *Planetary and Space Science*, 88, 64–75. <https://doi.org/10.1016/j.pss.2013.05.023>
- Bonfond, B., Saur, J., Grodent, D., Badman, S. V., Bisikalo, D., Shematovich, V., et al. (2017). The tails of the satellite auroral footprints at Jupiter. *Journal of Geophysical Research: Space Physics*, 122, 7985–7996. <https://doi.org/10.1002/2017JA024370>
- Brygoo, S., Loubeyre, P., Millot, M., Rygg, J. R., Celliers, P. M., Eggert, J. H., et al. (2021). Evidence of hydrogen–helium immiscibility at Jupiter-interior conditions. *Nature*, 593, 517–521. <https://doi.org/10.1038/s41586-021-03516-0>
- Cain, J. C., Wang, Z., Schmitz, D., & Meyer, J. (1989). The geomagnetic spectrum for 1980 and core-crustal separation. *Geophysical Journal*, 97, 443–447. <https://doi.org/10.1111/j.1365-246x.1989.tb00514.x>
- Cao, H., & Stevenson, D. J. (2017). Zonal flow magnetic field interaction in the semi-conducting region of giant planets. *Icarus*, 296, 59–72. <https://doi.org/10.1016/j.icarus.2017.05.015>
- Chapman, S., & Bartels, J. (1940). *Geomagnetism* (pp. 639–668). Oxford University Press.
- Chulliat, A., Macmillan, S., Alken, P., Beggan, C., Nair, M., Hamilton, B., et al. (2015). *The US/UK world magnetic model for 2015–2020: Technical report*. National Geophysical Data Center, NOAA. <https://doi.org/10.7289/V5TB14V7>
- Clarke, J. T., Ajello, J., Ballester, G. E., Jaffel, L. B., Connerney, J., Gérard, J. C., et al. (2002). Ultraviolet emissions from the magnetic footprints of Io, Ganymede, and Europa on Jupiter. *Nature*, 415, 997–1000.
- Connerney, J. E. P. (1981). The magnetic field of Jupiter: A generalized inverse approach. *Journal of Geophysical Research*, 86, 7679–7693. <https://doi.org/10.1029/ja086ia09p07679>
- Connerney, J. E. P. (1993). Magnetic fields of the outer planets. *Journal of Geophysical Research*, 98, 18659–18679. <https://doi.org/10.1029/93je00980>
- Connerney, J. E. P. (2015). Planetary magnetism. Volume 10: Planets and satellites. In G. Schubert, & T. Spohn (Eds.), *Treatise in geophysics* (Vol. 10.06, pp. 195–237). Elsevier. <https://doi.org/10.1016/b978-0-444-53802-4.00171-8>
- Connerney, J. E. P. (2017). Juno fluxgate magnetometer calibrated data V1.0 [Data set]. NASA Planetary Data System. <https://doi.org/10.17189/1519711>
- Connerney, J. E. P., & Acuña, M. H. (1982). Jovimagnetic secular variation. *Nature*, 297, 313–315. <https://doi.org/10.1038/297313a0>
- Connerney, J. E. P., Acuña, M. H., Ness, N. F., & Satoh, T. (1998). New models of Jupiter’s magnetic field constrained by the Io flux tube footprint. *Journal of Geophysical Research*, 103(A6), 11929–11939. <https://doi.org/10.1029/97ja03726>
- Connerney, J. E. P., Acuña, M. H., & Ness, N. F. (1981). Modeling the Jovian current sheet and inner magnetosphere. *Journal of Geophysical Research*, 86, 8370–8384. <https://doi.org/10.1029/ja086ia10p08370>
- Connerney, J. E. P., Acuña, M. H., & Ness, N. F. (1982). N.F. Voyager 1 assessment of Jupiter’s planetary magnetic field. *Journal of Geophysical Research*, 86, 3623–3627. <https://doi.org/10.1029/ja087ia05p03623>
- Connerney, J. E. P., Acuña, M. H., & Ness, N. F. (1996). Octupole model of Jupiter’s magnetic field from Ulysses observations. *Journal of Geophysical Research*, 101, 27453–27458. <https://doi.org/10.1029/96ja02869>
- Connerney, J. E. P., Baron, R., Satoh, T., & Owen, T. (1993). Images of excited H₃⁺ at the foot of the Io flux tube in Jupiter’s atmosphere. *Science*, 262, 1035–1038. <https://doi.org/10.1126/science.262.5136.1035>

- Connerney, J. E. P., Benn, M., Bjarno, J. B., Denver, T., Espley, J., Jorgensen, J. L., et al. (2017). The Juno magnetic field investigation. *Space Science Reviews*, 213, 39–138. <https://doi.org/10.1007/s11214-017-0334-z>
- Connerney, J. E. P., Kotsiaros, S., Oliverson, R. J., Espley, J. R., Joergensen, J. L., Joergensen, P. S., et al. (2018). A new model of Jupiter's magnetic field from Juno's first nine orbits. *Geophysical Research Letters*, 45, 2590–2596. <https://doi.org/10.1002/2018GL077312>
- Connerney, J. E. P., Timmins, S., Hecceg, M., & Joergensen, J. L. (2020). A Jovian magnetodisc model for the Juno era. *Journal of Geophysical Research: Space Physics*, 125, e2020JA028138. <https://doi.org/10.1029/2020JA028138>
- Conway, R. G., & Stannard, D. (1972). Non-dipole terms in the magnetic fields of Jupiter and the Earth. *Nature*, 239, 142–143. <https://doi.org/10.1038/physci239142a0>
- Dessler, A. J., & Hill, T. W. (1975). High order multipoles as a source of gross asymmetry in the distant Jovian magnetosphere. *Geophysical Research Letters*, 2, 567. <https://doi.org/10.1029/g1002i012p00567>
- Dessler, A. J., & Hill, T. W. (1979). Jovian longitudinal control of Io-related radio emissions. *The Astrophysical Journal*, 227, 664. <https://doi.org/10.1086/156777>
- Elphic, R. C., & Russell, C. T. (1978). On the apparent source depth of planetary magnetic fields. *Geophysical Research Letters*, 5, 211–214. <https://doi.org/10.1029/g1005i003p00211>
- French, M., Becker, A., Lorenzen, W., Nettleman, N., Bethkenhagen, M., Wicht, J., & Redmer, R. (2012). Ab initio simulations for material properties along the Jupiter adiabat. *The Astrophysical Journal Supplement*, 202(1), 5. <https://doi.org/10.1088/0067-0049/202/1/5>
- Gastine, T., & Wicht, J. (2021). Stable stratification promotes multiple zonal jets in a turbulent Jovian dynamo model. *Icarus*, 368, 114514. <https://doi.org/10.1016/j.icarus.2021.114514>
- Genova, F., & Aubier, M. G. (1985). Io-dependent sources of the Jovian decameter emission. *Astronomy & Astrophysics*, 150, 139–150.
- Grodent, D., Bonfond, B., Gérard, J.-C., Radioti, A., Gustin, J., Clarke, J. T., et al. (2008). Auroral evidence of a localized magnetic anomaly in Jupiter's northern hemisphere. *Journal of Geophysical Research*, 113, A09201. <https://doi.org/10.1029/2008JA013185>
- Guillot, T., Miguel, Y., Militzer, B., Hubbard, W. B., Kaspi, Y., Galanti, E., et al. (2018). A suppression of differential rotation in Jupiter's deep interior. *Nature*, 555, 227–230. <https://doi.org/10.1038/nature25775>
- Guillot, T., Stevenson, D. J., Hubbard, W. B., & Saumon, D. (2004). The interior of Jupiter. In F. Bagenal, T. Dowling, & W. McKinnon (Eds.), *Jupiter: The planet, satellites and magnetosphere*. Cambridge University Press.
- Hecceg, M., Jorgensen, P. S., Jorgensen, J. L., & Connerney, J. E. P. (2020). Thermo-elastic response of the Juno spacecraft's solar array/magnetometer boom and its applicability to improved magnetic field investigation. *Earth and Space Science*, 7, e2020EA001338. <https://doi.org/10.1029/2020EA001338>
- Hess, S. L. G., Bonfond, B., Zarka, P., & Grodent, T. (2011). Model of the Jovian magnetic field topology constrained by the Io auroral emissions. *Journal of Geophysical Research*, 116, A05217. <https://doi.org/10.1029/2010JA016262>
- Kaspi, Y., Galanti, E., Hubbard, W., Stevenson, D. J., Bolton, S. J., Less, L., et al. (2018). Jupiter's atmospheric jet streams extend thousands of kilometres deep. *Nature*, 555, 223–226. <https://doi.org/10.1038/nature25793>
- Kotsiaros, S., Connerney, J. E. P., Clark, G., Allegrini, F., Gladstone, G. R., Kurth, W. S., et al. (2019). Birkeland currents in Jupiter's magnetosphere observed by the polar-orbiting Juno spacecraft. *Nature Astronomy*, 3, 904–909. <https://doi.org/10.1038/s41550-019-0819-7>
- Kotsiaros, S., Connerney, J. E. P., & Martos, Y. (2020). Analysis of Eddy current generation on the Juno spacecraft in Jupiter's magnetosphere. *Earth and Space Science*, 7, e2019EA001061. <https://doi.org/10.1029/2019EA001061>
- Lanczos, C. (1961). *Linear differential operations* (p. 564). D. Van Nostrand.
- Langel, R. A., & Estes, R. H. (1982). A geomagnetic field spectrum. *Geophysical Research Letters*, 9, 250–253. <https://doi.org/10.1029/g1009i004p00250>
- Langlais, B., Amit, H., Larnier, H., Thebault, E., & Mocquet, A. (2014). A new model for the (geo)magnetic power spectrum with application to planetary dynamo radii. *Earth and Planetary Science Letters*, 401, 347–358. <https://doi.org/10.1016/j.epsl.2014.05.013>
- Lowes, F. J. (1974). Spatial power spectrum of the main geomagnetic field and extrapolation to the core. *Geophysical Journal of the Royal Astronomical Society*, 36, 717–730. <https://doi.org/10.1111/j.1365-246x.1974.tb00622.x>
- Martos, Y. M., Imai, M., Connerney, J. E. P., Kotsiaros, S., & Kurth, W. S. (2020). Juno reveals new insights into Io-related decameter radio emissions. *Journal of Geophysical Research: Planets*, 125, e2020JE006415. <https://doi.org/10.1029/2020JE006415>
- Moore, K. M., Bloxham, J., Connerney, J. E. P., Jørgensen, J. L., & Merayo, J. M. G. (2017). The analysis of initial Juno magnetometer data using a sparse magnetic field representation. *Geophysical Research Letters*, 44, 4687–4693. <https://doi.org/10.1002/2017GL073133>
- Moore, K. M., Cao, H., Bloxham, J., Stevenson, D. J., Connerney, J. E. P., & Bolton, S. J. (2019). Time variation of Jupiter's internal magnetic field consistent with zonal wind advection. *Nature Astronomy*, 3(8), 730–735. <https://doi.org/10.1038/s41550-019-0772-5>
- Moore, K. M., Yadav, R. K., Kulowski, L., Cao, H., Bloxham, J., Connerney, J. E. P., et al. (2018). A complex dynamo inferred from the hemispheric dichotomy of Jupiter's magnetic field. *Nature*, 561, 76–78. <https://doi.org/10.1038/s41586-018-0468-5>
- Mura, A., Adriani, A., Connerney, J. E. P., Bolton, S. J., Altieri, F., Bagenal, F., et al. (2018). Juno observations of spot structures and a split tail in Io-induced aurorae on Jupiter. *Science*, 361, 774–777. <https://doi.org/10.1126/science.aat1450>
- Nellis, W. (2000). Metallization of fluid hydrogen at 140 GPa (1.4 Mbar): Implications for Jupiter. *Planetary and Space Science*, 48, 671–677. [https://doi.org/10.1016/S0032-0633\(00\)00031-3](https://doi.org/10.1016/S0032-0633(00)00031-3)
- Nellis, W., Weir, S. T., & Mitchell, A. C. (1999). Minimum metallic conductivity of fluid hydrogen at 140 GPa (1.4 Mbar). *Physical Review B: Condensed Matter*, 59(5), 3434–3449. <https://doi.org/10.1103/physrevb.59.3434>
- Nellis, W., Weir, S. T., & Mitchell, A. C. (1996). Metallization and electrical conductivity of hydrogen in Jupiter. *Science*, 273, 936–938. <https://doi.org/10.1126/science.273.5277.936>
- Olson, P., & Christensen, U. R. (2006). Dipole moment scaling for convection-driven planetary dynamos. *Earth and Planetary Science Letters*, 250, 561–571. <https://doi.org/10.1016/j.epsl.2006.08.008>
- Porco, C. C., West, R. A., McEwen, A., Del Genio, A. D., Ingersol, A. P., Thomas, P., et al. (2003). Cassini imaging of Jupiter's atmosphere, satellites, and rings. *Science*, 299, 1541–1547. <https://doi.org/10.1126/science.1079462>
- Ridley, V. A., & Holme, R. (2016). Modeling the Jovian magnetic field and its secular variation using all available magnetic field observations. *Journal of Geophysical Research: Planets*, 121, 309–337. <https://doi.org/10.1002/2015JE004951>
- Russell, C. T., & Dougherty, M. K. (2010). Magnetic fields of the outer planets. *Space Science Reviews*, 152, 251–269. <https://doi.org/10.1007/s11214-009-9621-7>
- Salpeter, E. E. (1973). On convection and gravitational layering in Jupiter and in stars of low mass. *The Astrophysical Journal*, 181, L83–L86. <https://doi.org/10.1086/181190>
- Seidelmann, P. K., & Divine, N. (1977). Evaluation of Jupiter longitudes in System III (1965). *Geophysical Research Letters*, 4, 65–68. <https://doi.org/10.1029/GL004i002p00065>

- Simon, A. A., Tabataba-Vakili, F., Cosentino, R., Beebe, R. F., Wong, M. H., & Orton, G. S. (2018). Historical and contemporary trends in the size, drift, and color of Jupiter's great red spot. *The Astronomical Journal*, *155*, 151. <https://doi.org/10.3847/1538-3881/aaae01>
- Simon, A. A., Wong, M. H., & Orton, G. S. (2015). First results from the Hubble OPAL program: Jupiter in 2015. *The Astrophysical Journal*, *812*, 55. <https://doi.org/10.1088/0004-637X/812/1/55>
- Smoluchowski, R. (1967). Internal structure and energy emission of Jupiter. *Nature*, *215*, 691–695. <https://doi.org/10.1038/215691a0>
- Smoluchowski, R. (1975). Jupiter's molecular hydrogen layer and the magnetic field. *The Astrophysical Journal Letters*, *200*, 119–121. <https://doi.org/10.1086/181911>
- Stallard, T. S., Burrell, A. G., Melin, H., Fletcher, L. N., Miller, S., Moore, L., et al. (2018). Identification of Jupiter's magnetic equator through ionospheric emission. *Nature Astronomy*, *2*, 773–777. <https://doi.org/10.1038/s41550-018-0523-z>
- Stevenson, D. J. (1983). Planetary magnetic fields. *Reports on Progress in Physics*, *46*, 555–620. <https://doi.org/10.1088/0034-4885/46/5/001>
- Stevenson, D. J. (2020). Jupiter's interior as revealed by Juno. *Annual Review of Earth and Planetary Sciences*, *48*, 465–489. <https://doi.org/10.1146/annurev-earth-081619-052855>
- Tsang, Y. K., & Jones, C. A. (2020). Characterising Jupiter's dynamo radius using its magnetic energy spectrum. *Earth and Planetary Science Letters*, *530*, 115879. <https://doi.org/10.1016/j.epsl.2019.115879>
- Weir, S. T., Mitchell, A. C., & Nellis, W. J. (1996). Metallization of fluid molecular hydrogen at 140 CPa (1.4 Mbar). *Physical Review Letters*, *76*, 1860–1863. <https://doi.org/10.1103/physrevlett.76.1860>
- Yu, Z. J., Leinweber, H. K., & Russell, C. T. (2009). Galileo constraints on the secular variation of the Jovian magnetic field. *Journal of Geophysical Research*, *115*, E03002. <https://doi.org/10.1029/2009JE003492>